Photoluminescence spectra of point defects in semiconductors: Validation of first-principles calculations

Yu Jin, Marco Govoni, Gary Wolfowicz, Sean E. Sullivan, F. Joseph Heremans, David D. Awschalom, and Giulia Galli

Photoluminescence spectra of point defects in semiconductors: validation of first principles calculations

Yu Jin,[1] Marco Govoni,[2,3,*] Gary Wolfowicz,[3] Sean E. Sullivan,[3]

F. Joseph Heremans,[2,3] David D. Awschalom,[2,3,4] and Giulia Galli[1,2,3,†]

[1]*Department of Chemistry, University of Chicago,*

Chicago, Illinois 60637, United States

[2]*Pritzker School of Molecular Engineering,*

University of Chicago, Chicago, Illinois 60637, United States

[3]*Materials Science Division and Center for Molecular Engineering,*

Argonne National Laboratory, Lemont, Illinois 60439, United States

[4]*Department of Physics, University of Chicago,*

Chicago, Illinois 60637, United States

(Dated: August 9, 2021)

Abstract

Optically and magnetically active point defects in semiconductors are interesting platforms for the development of solid-state quantum technologies. Their optical properties are usually probed by measuring photoluminescence spectra, which provide information on excitation energies and on the interaction of electrons with lattice vibrations. We present a combined computational and experimental study of photoluminescence spectra of defects in diamond and SiC, aimed at assessing the validity of theoretical and numerical approximations used in first principles calculations, including the use of the Franck-Condon principle and the displaced harmonic oscillator approximation. We focus on prototypical examples of solid-state qubits, the divacancy centers in SiC and the nitrogen-vacancy in diamond, and we report computed photoluminescence spectra as a function of temperature that are in very good agreement with the measured ones. As expected we find that the use of hybrid functionals leads to more accurate results than semilocal functionals. Interestingly our calculations show that constrained density functional theory (CDFT) and time-dependent hybrid DFT perform equally well in describing the excited state potential energy surface of triplet states; our findings indicate that CDFT, a relatively cheap computational approach, is sufficiently accurate for the calculations of photoluminescence spectra of the defects studied here. Finally, we find that only by correcting for finite-size effects and extrapolating to the dilute limit, one can obtain a good agreement between theory and experiment. Our results provide a detailed validation protocol of first principles calculations of photoluminescence spectra, necessary both for the interpretation of experiments and for robust predictions of the electronic properties of point defects in semiconductors.

I. INTRODUCTION

The last two decades have witnessed the rapid development of quantum information technologies based on solid state platforms, in particular optically addressable spin-defects in semiconductors and insulators [1–4]. The opto-electronic properties of point defects used to realize qubits are most often probed by measuring photoluminescence (PL) spectra, which yield information about excitation energies and the interaction of the excited electrons with

* mgovoni@anl.gov

† gagalli@uchicago.edu

lattice vibrations.

A PL experiment collects the photons emitted when an excited electron radiatively decays to the ground state (GS), and PL spectra of defects usually exhibit a narrow zero-phonon line (ZPL) and a broad phonon side band (PSB); the latter originates from decay processes that involve structural relaxation and thus the coupling of electrons and phonons. The strength of such coupling can be inferred from the DebyeWaller factor (DWF) [5] that is proportional to the ratio between the emission intensity of the ZPL and that of the entire spectrum. Applications that require photon coherence or interference benefit from points defects whose PL signal exhibits a high DWF, indicating a weak coupling between phonons and electrons. The average number of phonons emitted during an electronic transition is instead quantified by the Huang-Rhys factor (HRF) [5, 6], which can be estimated from measured spectra from the logarithm of the DWF.

As for many properties of condensed systems, Density Functional Theory (DFT) has turned out to be a valuable tool to compute PL spectra, which are used to interpret experiments as well as to provide predictions of the fingerprints of specific defects in materials [7–9]. For example, first principles spectra based on DFT have been recently reported for nitrides, e.g., GaN [10, 11], AlN [12], and hexagonal born nitride (h-BN) [13–18], diamond [19–29], silicon carbide (SiC) [30–33], and monolayers of transition metal dichalcogenides (TMDC) [34]. These studies have been performed with several useful computational approaches; however, a systematic assessment of the theoretical and numerical approximations adopted in PL calculations has not yet been conducted.

In this work, we present a joint theoretical and experimental study of the PL spectra of prototypical spin-defects in diamond and SiC. We focus on the negatively charged nitrogen-vacancy (NV^-) in diamond [5, 35–39] and the neutral divacancy ($V_{Si}V_C^0$, abbreviated as VV^0) centers in hexagonal 4H-SiC which have been recently suggested as promising platforms for quantum sensors [40–43]. While the NV^- center has just one possible geometrical configuration in the GS, the VV^0 centers may attain four different geometries due to the layered structure of 4H-SiC, giving rise to different PL signals. We discuss the comparison between theoretical and experimental PL spectra as a function of temperature, as well as HRFs and DWFs, and we present a detailed assessment of the theoretical and numerical approximations involved in first principles calculations. These approximations include the choice of the density functional, the method adopted to describe excited state (ES) potential

energy surfaces, finite supercell size and approximations based on the Franck-Condon (FC) principle and the displaced harmonic oscillator (DHO) approximation.

We compare constrained DFT (CDFT) [44] calculations of ES potential energy surfaces of triplet states with those carried out with time-dependent DFT (TDDFT), which enable the description of the ES as a linear combination of multiple Slater determinants. In our TDDFT calculations we use hybrid functionals with the fraction of exact exchange determined by the dielectric constant of the system; based on recent studies, these calculations are expected to yield results in good agreement with the solutions of the Bethe-Salpeter equation [45, 46]. So far, TDDFT has only been employed to describe spin defects with cluster models and atomic centered basis sets [26, 29, 47–49] and here we present a comparison between CDFT and TDDFT calculations carried out for the same supercell and using the same plane-wave basis sets and density functional. We also investigate finite size effects which affect defect-host interactions and present results for PL line shapes converged to supercells with more than 10,000 atoms, following the approach proposed by Alkauskas et al. [19, 28, 50]. Finally, we provide a qualitative assessment of the accuracy of the FC principle and the the displaced harmonic oscillator (DHO) approximation. By conducting fully converged hybrid functional calculations for the electronic properties, we obtain good agreement with measured spectra over a wide temperature range, with small differences between PL line shapes obtained with phonons computed with semilocal or hybrid functionals.

The rest of the paper is organized as follows. In Sec. II we discuss the methodology for computing PL spectra using the Huang-Rhys (HR) theory within the generating function formulation, highlighting all theoretical and numerical approximations. In Sec. III, we give the details of first-principles calculations and experiments. In Sec. IV, results on the chosen defects in SiC and diamond, including ZPLs, HRFs, DWFs and PL line shapes are discussed. Conclusions are given in Sec. V.

II. THEORY AND COMPUTATIONAL METHODOLOGY

Based on Fermi's golden rule and the FC principle, the PL spectrum generated by the optical transitions from the ES to the GS potential energy surfaces, as a function of the
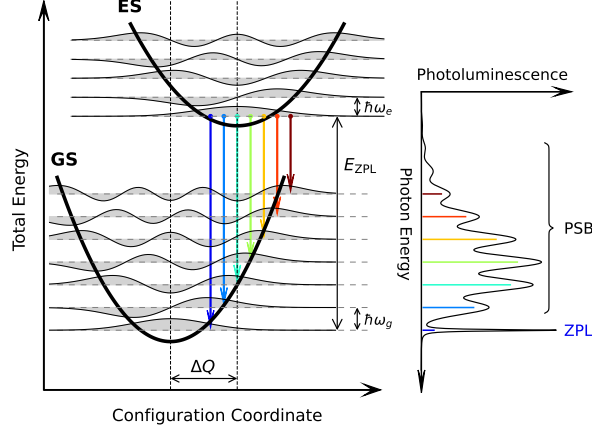
FIG. 1. Schematic diagram illustrating optical processes leading to photoluminescence (PL) spectra. For simplicity only one phonon mode is depicted in the diagram. Ground state (GS) and excited state (ES) potential energy curves are approximated by harmonic functions with frequency ω_g and ω_e, respectively. Vibrational energy levels and wavefunctions are shown as horizontal dashed lines and gray areas, respectively. ΔQ is the mass-weighted displacement between the local minimum of the GS and the ES energy curves. Colored arrows represent optical transitions at 0 K. The zero-phonon line (ZPL) originates from the transition between the 0-th vibrational level of the ES to the 0-th vibrational level of the GS. All other transitions contribute to the phonon sideband (PSB).

photon energy $\hbar\omega$, is expressed as [19]:

$$L(\hbar\omega, T) = \frac{n\omega^3}{3\pi\epsilon_0 c^3\hbar} \left|\boldsymbol{\mu}_{eg}\right|^2 \sum_i \sum_j P_{ej}(T) \left|\langle \Theta_{ej} \mid \Theta_{gi}\rangle\right|^2 \delta\left(E_{\mathrm{ZPL}} + E_{ej} - E_{gi} - \hbar\omega\right), \quad (1)$$

where $\boldsymbol{\mu}_{eg}$ is the electronic transition dipole moment; n is the refractive index of the material; $|\Theta^{gi}\rangle$ ($|\Theta^{ej}\rangle$) is the i-th (j-th) nuclear wavefunction of the system in the GS (ES) with vibrational energy E_{gi} (E_{ej}); E_{ZPL} is the energy of the ZPL (see Fig. 1). The thermal distribution function of the vibrational energy in the ES is

$$P_{ej}(T) = \frac{e^{-\frac{E_{ej}}{k_B T}}}{\sum_j e^{-\frac{E_{ej}}{k_B T}}}, \quad (2)$$

where k_B is the Boltzmann constant. For an ordered solid, under the harmonic approximation we express the nuclear wavefunctions as products of vibrational wavefunctions:

$$|\Theta_{gi}\rangle = \prod_k |\phi_{k n_k^{gi}}\rangle, \quad |\Theta_{ej}\rangle = \prod_k |\phi_{k n_k^{ej}}\rangle, \quad (3)$$

5

where n_k^{gi} (n_k^{ej}) is the number of k-th phonons in the i-th (j-th) vibrational state of the GS (ES), and $|\phi_{kn}\rangle$ is the n-th excited state of the k-th phonon mode. The vibrational energies in the GS and ES are:

$$E_{gi} = \sum_k n_k^{gi}\hbar\omega_k^g, \quad E_{ej} = \sum_k n_k^{ej}\hbar\omega_k^e, \tag{4}$$

where ω_k^g (ω_k^e) is the frequency of k-th phonon in the GS (ES). Note that by definition Eq. 4 does not include the zero point energy which is included in the term E_{ZPL}.

A commonly used approximation is the so called displaced harmonic oscillator (DHO) approximation, (or HR theory [6]), where Eq. 1 is simplified by assuming that the potential energy surface of the ES and the GS are identical except for a rigid displacement due to the difference in their equilibrium structures, i.e., $\omega_k^g = \omega_k^e$ (the superscript g and e will hence be omitted), and:

$$|\langle\Theta_{ej}\,|\,\Theta_{gi}\rangle|^2 = \prod_k e^{-S_k}(S_k)^{n_k^{gi}-n_k^{ej}}\left(\frac{n_k^{ej}!}{n_k^{gi}!}\right)\left[L_{n_k^{ej}}^{n_k^{gi}-n_k^{ej}}(S_k)\right]^2, \tag{5}$$

where S_k is the partial HRF and accounts for the average number of k-th phonons that participate in the transition. L_m^{n-m} are the associated Laguerre polynomials [51]. For the calculations of PL line shapes, only the phonons of the GS are computed and used within the DHO approximation. At zero temperature, Eq. 1 may be further approximated by setting to zero the vibrational energy in the ES (i.e., we only consider $j=0$, and $n_k^{e0}=0$), namely:

$$L(\hbar\omega, T=0) \propto \omega^3 \sum_i \left[\prod_k \frac{e^{-S_k}}{n_k^{gi}!}(S_k)^{n_k^{gi}}\right]\delta\left(E_{ZPL} - E_{gi} - \hbar\omega\right). \tag{6}$$

To avoid the evaluation of the overlap integrals entering Eq. 5 and the sum over all vibrational states of the GS and the ES, we adopt the generating function approach [52, 53] to compute PL spectra. In the DHO approximation Eq. 1 can be obtained as the Fourier transform of the generating function $G(t, T)$:

$$L(\hbar\omega, T) \propto \omega^3 \int_{-\infty}^{\infty} \mathrm{d}t\, G(t, T)e^{i\omega t - \frac{\lambda}{\hbar}|t| - i\frac{E_{\mathrm{ZPL}}}{\hbar}t}, \tag{7}$$

where

$$G(t, T) = \exp\left\{-\sum_k S_k\left[\left(1 - e^{i\omega_k t}\right) + \bar{n}_k(T)\left(2 - e^{i\omega_k t} - e^{-i\omega_k t}\right)\right]\right\}, \tag{8}$$

and λ accounts for the broadening of the line shape. $\bar{n}_k(T)$ is the average occupation number of the k-th phonon mode:

$$\bar{n}_k(T) = \frac{1}{e^{\frac{\hbar\omega_k}{k_B T}} - 1}. \tag{9}$$

6

In practice, one may write Eq. 8 as the following alternative expression:

$$G(t,T) = e^{S(t)-S(0)+C(t,T)+C(-t,T)-2C(0,T)}, \tag{10}$$

where $S(t) = \sum_k S_k e^{i\omega_k t}$ and $C(t,T) = \sum_k \bar{n}_k(T) S_k e^{i\omega_k t}$ are evaluated as the Fourier transforms of the spectral densities:

$$S(\hbar\omega) = \sum_k S_k \delta(\hbar\omega - \hbar\omega_k), \tag{11}$$

$$C(\hbar\omega,T) = \sum_k \bar{n}_k(T) S_k \delta(\hbar\omega - \hbar\omega_k). \tag{12}$$

In Eqs. 11-12, the δ-functions are replaced by Gaussian functions with ω-dependent broadening to account for a continuum of vibrational modes participating in the optical transition (see Sec. IV B).

At zero temperature, we have $\bar{n}_k(T=0) \approx 0$ and $C(\hbar\omega, T=0) \approx 0$, and Eq. 7 is equivalent to Eq. 6 with the δ-function replaced by a Lorentzian function with a broadening λ. In order to evaluate Eq. 7, the partial HRF S_k, E_{ZPL}, and phonon frequencies ω_k are required as input. We compute S_k as:

$$S_k = \frac{\omega_k \Delta Q_k^2}{2\hbar}, \tag{13}$$

where ΔQ_k is the mass-weighted displacement along the k-th mode, evaluated as:

$$\Delta Q_k = \sum_{\alpha=1}^{N} \sum_{i=x,y,z} \sqrt{M_\alpha} \Delta \mathbf{R}_{\alpha i} \boldsymbol{e}_{k,\alpha i}. \tag{14}$$

In Eq. 14, $\mathbf{e}_{k,\alpha i}$ is the eigenvector of the k-th phonon mode on the α-th atom in the i-th direction; M_α is the mass of the α-th atom, and $\Delta \mathbf{R}_{\alpha i} = (\mathbf{R}_{\alpha i})_e - (\mathbf{R}_{\alpha i})_g$ is the displacement between the ES and the GS equilibrium atomic structures in the i-th direction. Within the harmonic approximation, ΔQ_k may be equivalently computed as [19]:

$$\Delta Q_k = \frac{1}{\omega_k^2} \sum_{\alpha=1}^{N} \sum_{i=x,y,z} \frac{\mathbf{F}_{\alpha i}}{\sqrt{M_\alpha}} \boldsymbol{e}_{k,\alpha i}. \tag{15}$$

Here $\mathbf{F}_{\alpha i}$ is the GS force on the α-th atom in the i-th direction evaluated at the ES equilibrium structure.

In this work, we simulate PL spectra at finite temperature using Eq. 7, with parameters computed from first principles. In particular, we use DFT to obtain the GS equilibrium

atomic structure, $\mathbf{R}_g$, the GS forces, $\mathbf{F}$, the phonon modes, $\mathbf{e}$, and the phonon frequencies ω; the ES equilibrium atomic structure, $\mathbf{R}_e$, is obtained with CDFT and, in some cases validated by carrying out TDDFT calculations. The resulting PL line shapes are then compared with measured PL spectra at finite temperature. Below, we report our results and we systematically investigate the validity of the chosen theoretical and numerical approximations, including the use of the FC and the DHO approximations, which are at the core of the HR theory.

III.   TECHNICAL DETAILS

A.   First principles calculations

The electronic structures of the defects in diamond and 4H-SiC are obtained using DFT and the planewave pseudopotential method, as implemented in the Quantum Espresso package [54–56]. The planewave energy cutoff was set to 80 Ry. We used SG15 ONCV norm-conserving pseudopotentials [57, 58] and the semi-local functional by Perdew, Burke, and Ernzerhof (PBE) [59], the dielectric dependent hybrid (DDH) functional [60] and the screened hybrid functional by Heyd, Scuseria, and Ernzerhof (HSE) [61, 62]. The fraction of exact exchange used in the DDH functional was determined by the inverse of the macroscopic dielectric constant of the system, resulting in 18% and 15% of exact exchange for diamond and 4H-SiC [60, 63], respectively. The macroscopic dielectric constants were computed by including the full response of the electronic density to the perturbing external electric field at the level of hybrid functional, and the fraction of exact exchange was self-consistently determined from the dielectric constant [60].

We used a $(4 \times 4 \times 4)$ supercell with 512 atomic sites and a $(5 \times 5 \times 2)$ supercell with 400 atomic sites for the NV^- center in diamond and VV^0 centers in 4H-SiC, respectively. In the cases of VV^0 centers in 4H-SiC, convergence tests were carried out with large supercells (up to $(8 \times 8 \times 2)$). We used the lattice constant optimized with each specific functional (see Tab. S1 of the Supplementary Information (SI) [64]). The Brillouin zone was sampled with the Γ point.

The paramagnetic ESs were computed using the CDFT (also called ΔSCF) method, where one electron is promoted from the highest occupied to the lowest unoccupied state in

8

the same spin channel (see Sec. II of the SI for details of CDFT calculations). The energy E_{ZPL} was computed as the difference of the total energy of the relaxed ES (with CDFT) and that of the GS. The CDFT method has been shown to yield reliable results for systems with localized electronic states, e.g., the NV^- center in diamond [44] and VV^0 centers in 4H-SiC [33, 42, 65]. We also performed TDDFT calculations within the Tamm-Dancoff approximation to assess the accuracy of our CDFT results. We obtained the ES low-lying energies and eigenvectors by iteratively diagonalizing the linearized Liouville operator, as implemented in the WEST code [66, 67]. Due to the higher computational cost of TDDFT calculations, we used a $(3 \times 3 \times 3)$ supercell and a $(5 \times 3\sqrt{3} \times 1)$ supercell for the NV^- center in diamond and VV^0 centers in 4H-SiC, respectively.

Phonon modes of bulk and defective solids were computed using the frozen phonon approach, with configurations generated with the PHONOPY package [68] and a displacement of 0.01 Å from equilibrium structures. Phonon calculations for pristine bulk systems were carried out with the PBE, DDH and HSE functionals, but those for defective solids were performed only with PBE due to the high computational cost of hybrid functionals. We then approximated the values of hybrid-DFT phonons by using a scaling factor equal to the ratio of hybrid-DFT and PBE phonon results in the pristine bulk systems. We verified that this approximation yields accurate phonon frequencies for bulk systems (see Sec. IV of the SI for details). We evaluated finite size effects on computed PL line shapes, HRFs and spectral densities following the force constant matrix embedding approach proposed by Alkauskas et al. [19, 28, 50] (see Sec. V of the SI).

B. Experiments

The SiC experiments were realized in a confocal microscopy setup (0.67 NA objective) with the sample in a closed-cycle cryostat at 10 K, unless mentioned otherwise. The sample was diced from a commercial high-purity semi-insulating 4H-SiC wafer (Cree) containing intrinsic concentrations of VV^0 (10^{15}-10^{16} cm^{-3}). The sample was excited within the VV^0 absorption sideband with a 908 nm laser (QPhotonics, $\sim$100 mW), and the resulting PL was filtered using several 1000 nm long-pass filters. The PL was then measured using a spectrometer with a 300 g/mm grating blazed for 1.2 μm and an InGaAs camera (Teledyne Princeton Instruments) with a spectral resolution of $\sim$0.3 nm. Careful calibration was

performed to correct for the entire setup transmission and the camera response using a NIST calibrated tungsten-halogen white light source (StellarNet). Optically-detected magnetic resonance at a weak static magnetic field (<20 G) with microwave excitation delivered using a printed circuit board was used to obtain independent contrast (i.e., the difference in PL with and without microwave excitation) for the various VV^0 sites. The DWF is calculated as the ratio of the integrated intensity of the ZPL to the total integrated intensity. Though most of the PL is within our detection bandwidth (900-1600 nm), the sideband may be very slightly underestimated due to weak emission extending beyond this range.

Similarly, for the NV^- center in diamond, the PL spectra were taken on an ensemble of NV^- centers using a home-built confocal microscope with a flow cryostat (Janis - LakeShore Cryotronics) for temperature studies. The sample was a IB diamond (Sumitomo) with a high nitrogen concentration synthesized via high-pressure / high-temperature growth. The sample was electron irradiated (2 MeV, 10^{17} cm^{-2}) and annealed (850 C, 2 hr) resulting in a high density of NV^- centers. The NV^- center ensemble was photo-excited within the absorption sideband using 532 nm light and the PL measurements were collected using a high resolution spectrometer with a visible camera (Teledyne Princeton Instruments) with $\sim$0.1 nm spectral resolution. The spectrum intensity was also calibrated using a tungsten halogen light source (Ocean Optics) to correct for transmission losses in the experimental set-up.

IV. RESULTS AND DISCUSSION

A. Zero-phonon lines

The NV^- center in diamond is composed of a nitrogen impurity and an adjacent carbon vacancy (V_C) with an additional electron, as shown in Fig. 2(a) [37, 38]. It has C_{3v} symmetry, and three defect orbitals are present within the band gap of diamond: the a_1 orbital and the two-fold degenerate e orbitals, as shown in Fig. 3(a). Defect orbitals are mainly localized on three carbon atoms around the V_C (see Fig. S1 of the SI).

The neutral divacancy center in 4H-SiC is composed of a silicon vacancy (V_{Si}) and an adjacent carbon vacancy (V_C) and is denoted as $V_{Si}V_C^0$ [40, 41]. We consider the 4H polytype of SiC, 4H-SiC, with ABCB stacking along the c-axis. 4H-SiC contains two nonequivalent

hexagonal (h) and quasi-cubic (k) sites for each type of atom, as shown in Fig. 2(b). There-fore, the VV^0 center can occur in four distinct configurations (hh, kk, hk and kh), and the experimentally measured PL ensemble is a mixture of contributions from all configurations. Experimentally, we used microwave-assisted spectroscopy to separate the PL of different configurations. In our computational study, we considered the hh, kk, and hk configurations denoted as hh-VV^0, kk-VV^0 and hk-VV^0. The first two c-axis orientated defects (hh-VV^0 and kk-VV^0) have C_{3v} symmetry, with an a_1 state and two sets of degenerate e states within the band gap of 4H-SiC (see Fig. 3(b)). The a_1 orbital and lower e orbitals are mainly localized on three carbon atoms around the V_{Si} (see Fig. S1 of the SI). For NV^-, hh-VV^0 and kk-VV^0, we studied the optical transition between the a_1 orbital and the (lower) e orbitals, which corresponds to the transition between the $^3A_2$ and the ^3E many-body states. For the hk configuration, which has C_{1h} symmetry, we studied the a' and the a'' transition accounting for the transition between the $^3A''$ and the $^3A'$ state.

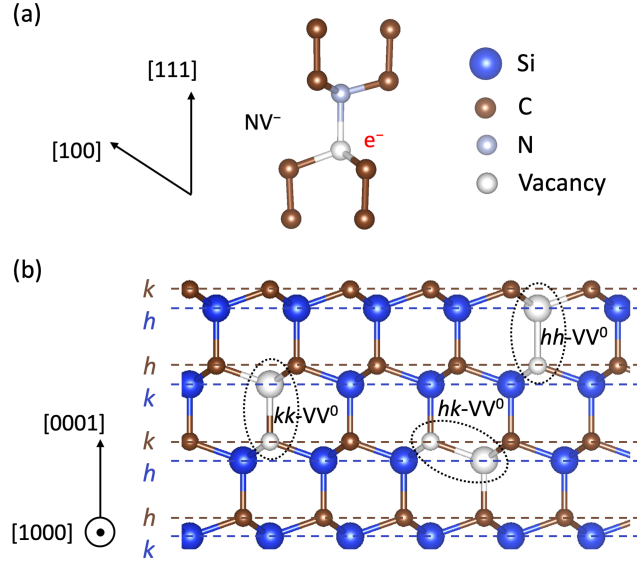We computed E_{ZPL} using the PBE, DDH, and HSE functionals in the DHO approxima-

FIG. 2. Ball and stick representation of the defect centers studied in this work. (a) NV^- center in diamond. (b) Divacancy ($V_{Si}V_C^0$) centers in 4H-SiC. The planes are labelled with h and k according to the symmetry of lattice sites. Three non-equivalent configurations (hh, kk and hk) of the $V_{Si}V_C^0$ centers are shown. The kh configuration was not investigated computationally, due to the lower quality of the experimental spectrum for this configuration.
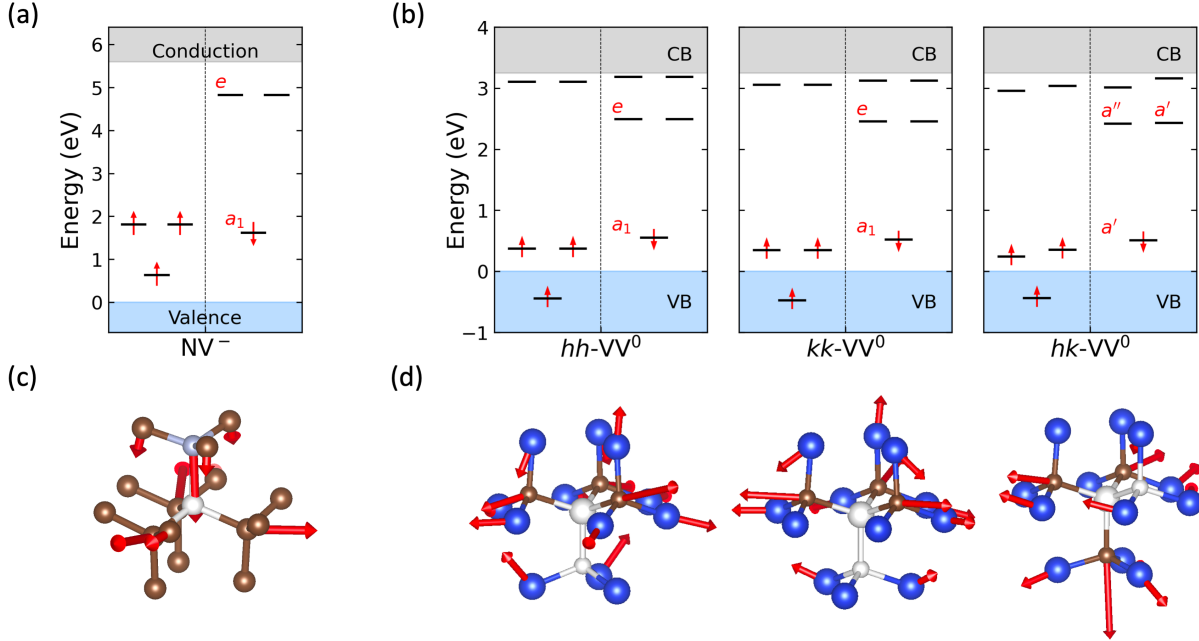
11

FIG. 3. Ground state (GS) electronic structure of (a) NV$^-$ center in diamond and (b) VV^0 centers in 4H-SiC at the DDH level of theory. Displacements between the excited state (ES) and the GS equilibrium structures of the NV$^-$ center in diamond and the VV^0 centers in 4H-SiC are shown in (c) and (d), respectively. The red arrows represent mass-weighted displacements (ΔQ) of each atom with the magnitude being amplified by a factor of 10. The ΔQ of the NV$^-$ center is mainly localized on the nitrogen atom and three nearest neighbor carbon atoms around the carbon vacancy. The ΔQ of the VV^0 centers is mainly localized on three nearest neighbor carbon atoms and nine next nearest neighbor silicon atoms around the silicon vacancy, as well as three nearest neighbor silicon atoms around the carbon vacancy.

tion (note that the zero-point energy contributions of the GS and ES phonons cancel out within the DHO approximation). Triplet ESs were computed using CDFT with electronic configuration $a_1^1 e_x^2 e_y^1$ (see Sec. II of the SI for details of CDFT calculations). Results for all defect systems at different levels of theory are summarized in Tab. I. The PBE functional underestimates the measured E_{ZPL} of the NV$^-$ by 0.24 eV, while the DDH and HSE functionals overestimate it by 0.26 eV. In the case of VV^0 centers, particular attention must be exercised to account for finite size effects. For small cells (e.g. $(5 \times 5 \times 2)$ supercell), the experimental order of the ZPL of the various defect configurations is not reproduced. Hence we computed E_{ZPL} at the PBE level of theory for $(5 \times 5 \times 2)$ and $(8 \times 8 \times 2)$ supercells; we

then used the difference between these two values to estimate the converged hybrid-DFT E_{ZPL} starting from our results obtained with $(5 \times 5 \times 2)$ supercells. The converged results reproduce the experimental trend. Similar to our results for diamond, we find that the PBE functional underestimates the measured E_{ZPL} of the VV^0 centers by ~ 0.16 eV, while the DDH (HSE) yields an overestimate of ~ 0.11 eV (~ 0.12 eV). Tab. I summarizes our results and previously reported theoretical predictions of E_{ZPL}. We note that although the E_{ZPL} obtained with the HSE functional is generally in good agreement with experiments, theoretical results exhibit a variance up to 0.3 eV due to different choices of pseudopotentials, supercell sizes and sampling of the reciprocal space.

To estimate the accuracy of CDFT for the ES potential energy surface, we compared results obtained with CDFT and TDDFT for NV^-, hh-VV^0, and kk-VV^0 at the DDH level of theory. TDDFT enables the description of the ES as a linear combination of multiple Slater determinants. In our TDDFT calculations we use hybrid functionals with the fraction of exact exchange determined by the dielectric constant of the system; based on recent studies, these calculations are expected to yield results in good agreement with the solutions of the Bethe Salpeter equation [45, 46]. Previous TDDFT studies of these defect systems used cluster models and atomic-centered basis sets [26, 47, 48]. Here we consistently compared TDDFT and CDFT calculations performed with the same basis set and pseudopotential, in the same cell and with the same functional. After obtaining the equilibrium structure of the ES using the CDFT approach, we selected several configurations along the linear path connecting equilibrium atomic structures of the GS and the ES, and carried out single-point DFT, CDFT, and TDDFT calculations, from which configuration coordinate diagrams were obtained, as shown in Fig. 4. The comparison between TDDFT and CDFT results was carried out using the configuration $a_1^1 e_x^{1.5} e_y^{1.5}$ in CDFT because we could not converge the conguration $a_1^1 e_x^2 e_y^1$ when using the DDH functional. The difference between CDFT calculations at the PBE level using the $a_1^1 e_x^2 e_y^1$ and $a_1^1 e_x^{1.5} e_y^{1.5}$ electronic configurations is ~ 0.04 eV; assuming an energy difference of the same order of magnitude at the DDH level, we deemed the CDFT/TDDFT comparison with the $a_1^1 e_x^{1.5} e_y^{1.5}$ configuration to be a meaningful one. We found that the TDDFT energies of the ^3E states are 0.1 (0.04) eV smaller than CDFT energies for NV^- (VV^0); the minimum of the TDDFT curve is close to that of the CDFT curve, with a difference smaller than 6% for all three systems. An analysis of our TDDFT results shows that the spin-conserving transition between the a_1 and the e orbitals

13

TABLE I. Energy of the zero-phonon line (E_{ZPL}, eV) for spin-conserving transitions computed using different levels of theory and a $(4 \times 4 \times 4)$ supercell for the NV$^-$ center in diamond, and a $(5 \times 5 \times 2)$ supercell for the VV^0 centers in 4H-SiC. The extrapolation value of the E_{ZPL} with the finite size corrections is reported in parentheses. The finite size corrections are calculated as the difference of E_{ZPL} values between the $(8 \times 8 \times 2)$ and the $(5 \times 5 \times 2)$ supercell at the PBE level of theory. Previous theoretical predictions on E_{ZPL} are also shown.

Hosts	Defects	This work			Previous Theoretical Work			Expt.
		PBE	DDH	HSE	PBE	DDH	HSE	
Diamond	NV$^-$	1.706	2.205	2.205	1.72[a], 1.706[b]	2.22[a]	2.23[a], 1.955[b]	1.945 [37]
4H-SiC	hh-VV^0	1.086 (0.937)	1.346 (1.196)	1.371 (1.221)	1.03[a], 0.92[c]	1.30[a]	1.33[a], 1.056[c], 1.13[d], 1.14[e]	1.095
	kk-VV^0	1.105 (0.951)	1.355 (1.201)	1.372 (1.218)	0.94[c]		1.044[c], 1.14[d]	1.096
	hk-VV^0	1.075 (0.979)	1.355 (1.259)	1.365 (1.269)	0.97[c]		1.103[c], 1.21[d]	1.149

[a] Ref. [63]: Calculations were carried out using the Quantum Espresso package with ONCV pseudopotentials (PPs). The planewave energy cutoff was set to 75 Ry. The Brillouin zone was sampled with the Γ point. A $(4 \times 4 \times 4)$ (($5 \times 3\sqrt{3} \times 1$)) supercell was used for NV$^-$ (hh-VV^0).

[b] Ref. [44]: Calculations were carried out using the VASP code with PAW PPs. The planewave energy cutoff was set to 420 eV. The Brillouin zone was sampled with the Γ point. A $(4 \times 4 \times 4)$ supercell was used for NV$^-$.

[c] Ref. [42]: Calculations were carried out using the VASP code with PAW PPs. The Brillouin zone was sampled with the Γ point. A $(10 \times 10 \times 3)$ (($8 \times 8 \times 3$)) supercell was used for PBE (HSE) calculations. HSE E_{ZPL} was computed with PBE structure.

[d] Ref. [65]: Calculations were carried out using the VASP code with PAW PPs. The planewave energy cutoff was set to 400 eV. The Brillouin zone was sampled using a $2 \times 2 \times 2$ k-point mesh. A $(4 \times 3 \times 1)$ supercell was used for VV^0.

[e] Ref. [33]: Calculations were carried out using the VASP code with PAW PPs. The planewave energy cutoff was set to 400 eV. The Brillouin zone was sampled with the Γ point. A $(5 \times 5 \times 2)$ supercell was used for VV^0. HSE E_{ZPL} was computed with PBEsol structure.

contributes by more than 95% to the whole transition to the ^3E state, indicating that the ^3E state can be well-described by a single Slater determinant. This finding is in good agreement with that of a previous TDDFT study using a cluster model, atom-centered basis sets and the PBE0 functional [47]. We note that the quality of the agreement between TDDFT and CDFT depends on the functional and the system. For example, we found a difference of $\sim$0.2 eV in the excitation energy and a difference greater than 12% in the configuration coordinate of the minimum between TDDFT and CDFT results when using the PBE functional (see Fig. S3 of the SI). In addition, in the case of defect systems with singlet GS and ES, we expect non-negligible differences between TDDFT and CDFT results, since the accurate description of a singlet ES requires a linear combination of at least two Slater determinants [14, 69]. In that case the use of quantum embedding theories (QDET), should be preferable to describe strongly correlated states [70–72].

To understand the effect of lattice vibrations on optical transitions, we analyzed in detail the mass-weighted displacement ΔQ computed at different levels of theory (see Sec. III of the SI). The magnitude of the displacement follows the relation: HSE > DDH > PBE and the difference of the results obtained with different functionals can be up to 10%. The same trend can also be found for energies of bulk phonons, and can be understood by noting that the bonds in the diamond and SiC crystals turn out to be stiffer with HSE than with DDH, which are in turn stiffer than with PBE, as reflected in the difference of predicted lattice constants (see Tab. S1 of the SI). ΔQ is localized on the neighboring atoms of the defect center, as shown in Fig. 3(c) and (d), consistent with the localization of defect orbitals involved in the optical transition. We also found that the symmetry of the ES is reduced from C_{3v} to C_{1h} for NV$^-$, hh-VV^0 and kk-VV^0, and hence in principle both a_1 type and e type phonons could participate in the optical process. Although the average symmetry of the ES structure turns out to be C_{3v} due to the dynamic Jahn-Teller effect [22, 73], here we used the ES equilibrium structure with C_{1h} symmetry to include the coupling with e type phonons. Hence the ES configuration used is $a_1^1 e_x^2 e_y^1$.

B. Huang-Rhys factor and spectral density of the electron-phonon coupling

Tab. II summarizes HRFs computed using Eq. 13 at different levels of theory and includes combinations of mass-weighted displacements, ΔQ_k, computed with DDH or HSE

and phonons computed with PBE. We used a scaling factor (see Sec. IV of the SI) to approximate DDH (HSE) phonon frequencies using PBE results; the factor was evaluated from the ratio of frequencies of bulk systems optical phonons computed at different levels of theory, an approximation that introduces a root-mean-square error (RMSE) of only 0.4 meV for bulk 4H-SiC.

We find that the HRFs computed with the PBE functional are smaller than those com-
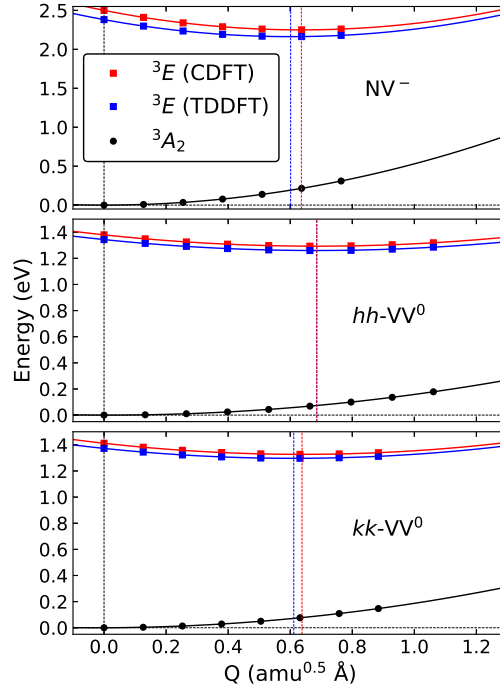

FIG. 4. Configuration coordinate diagrams describing the total energies of the $^3A_2$ ground state (GS) and the ^3E excited state (ES) along the relaxation path resulting from CDFT with electronic configuration $a_1^1 e_x^{1.5} e_y^{1.5}$ for the NV$^-$ center in diamond and the hh-VV^0 and the kk-VV^0 centers in 4H-SiC. Calculations are performed at the DDH level of theory. Dashed vertical lines denote the locations of the local minimum by fitting the energy curves with quadratic functions. The energy of the effective phonon obtained from the fitting process is 66.4 meV for the $^3A_2$ state and 72.0 (71.1) meV for the ^3E state, when computed with CDFT (TDDFT) for NV$^-$. The energy of the effective phonon is 36.8 meV for the $^3A_2$ state and 39.3 (38.6) meV for the ^3E state, when computed with CDFT (TDDFT) for hh-VV^0. The energy of the effective phonon is 38.7 meV for the $^3A_2$ state and 41.7 (41.2) meV for the ^3E state, when computed with CDFT (TDDFT) for kk-VV^0.

16

TABLE II. Huang-Rhys factors (HRFs) for spin-conserving transitions computed using Eq. 13 with different levels of theory. $PBE-\Delta Q$ denotes that ΔQ used in Eq. 13 is computed using Eq. 15 with forces and phonons computed at the PBE level. $PBE-ph$ denotes that phonons used in Eq. 13 are computed at the PBE level. Similar notations are used for DDH and HSE. Only one digit was kept for HRFs computed with the largest supercells considering the uncertainty introduced in the extrapolation procedure (see Sec. V of the SI). Experimental HRFs for VV^0 centers are estimated as the negative logarithm of the Debye-Waller factor (DWF).

Hosts	Defects	Cell Size	$PBE-\Delta Q$	$DDH-\Delta Q$		$HSE-\Delta Q$		Expt.
			$PBE-ph$	$PBE-ph$	$DDH-ph$	$PBE-ph$	$HSE-ph$	
Diamond	NV^-	$(4 \times 4 \times 4)$	2.94	3.20	3.32	3.46	3.64	3.49 [35]
		$(12 \times 12 \times 12)$	3.0	3.2	3.3	3.5	3.7	3.49 [35]
4H-SiC	hh-VV^0	$(5 \times 5 \times 2)$	2.55	2.55	2.64	2.72	2.86	3.30
		$(16 \times 16 \times 5)$	3.0	3.0	3.0	3.2	3.3	3.30
	kk-VV^0	$(5 \times 5 \times 2)$	2.51	2.53	2.62	2.68	2.81	2.80
		$(16 \times 16 \times 5)$	2.6	2.6	2.7	2.8	2.9	2.80
	hk-VV^0	$(5 \times 5 \times 2)$	2.26	2.46	2.54	2.53	2.66	2.58
		$(16 \times 16 \times 5)$	2.5	2.7	2.8	2.8	2.9	2.58

puted with hybrid functionals, consistent with the magnitude of the structural relaxations upon optical excitation (see Tab. S2 of the SI). In addition, the HRFs computed with hybrid functionals are larger when phonons are obtained at the DDH (HSE) level, consistent with the fact that the phonon frequencies computed with hybrid functionals are higher than those obtained at the PBE level of theory.

The spectral densities of electron-phonon coupling (Eq. 11) are computed with the $(4 \times 4 \times 4)$ supercell for NV^- and the $(5 \times 5 \times 2)$ supercell for VV^0 centers and shown in Fig. 5(a) and (c). The hybrid-DFT peak intensity is higher than that computed with PBE, consistent with the values of the HRF. As for spectral densities at the level of hybrid functionals, we find that peak positions are shifted to higher energies, compared with the PBE results, when phonons are computed with hybrid functionals.

In order to evaluate finite size effects on the HRFs and spectral densities, we need to compute ΔQ_k for large supercells with either Eq. 14 or Eq. 15. For the smallest supercell,
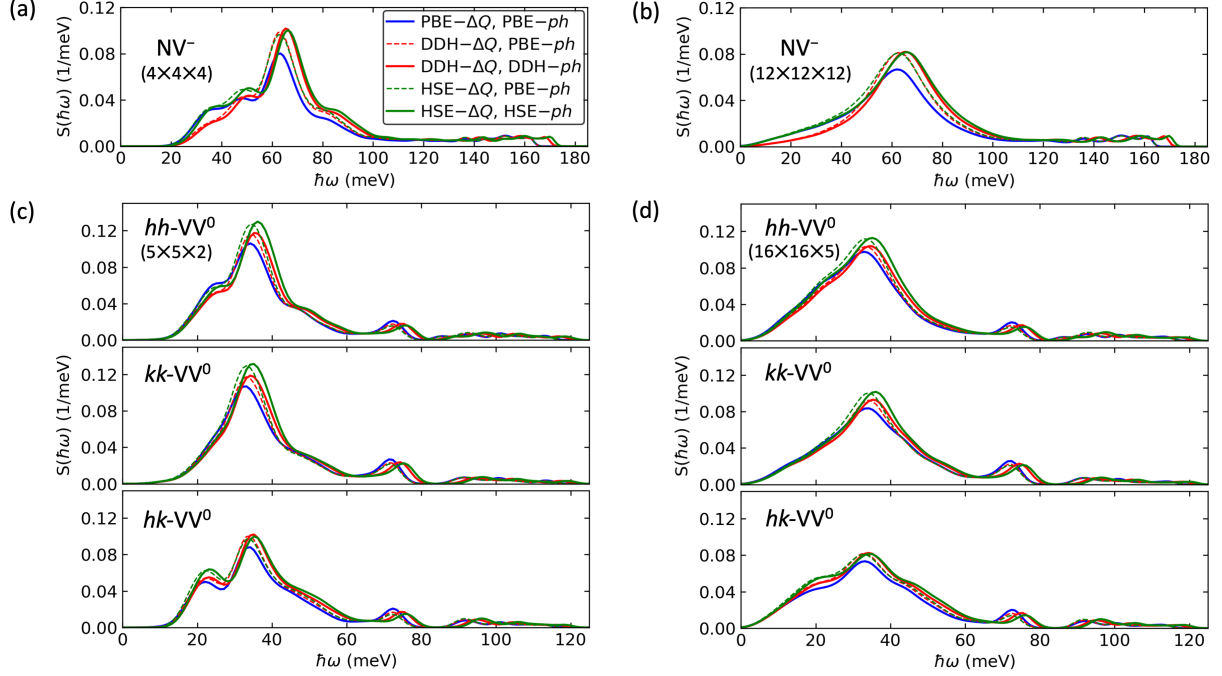
FIG. 5. Spectral densities of the electron-phonon coupling, $S(\hbar\omega)$, for defect systems computed at different levels of theory. The labels follow the same notation as in Tab. II. Gaussian functions with varying standard deviation (σ) were used to broaden the δ-function in Eq. 11. For the NV$^-$ center (VV^0 centers), σ is chosen to vary linearly from 6 (3.5) meV for the lowest-energy phonon to 1.5 (1.5) meV for the highest-energy phonon.

Eq. 14 and Eq. 15 yield results that differ by less than 3% (see Fig. S6 of the SI); hence for larger supercells we used Eq. 15 which converges more rapidly as a function of the distance from the defect center due to the fact that inter-atomic interactions in diamond and 4H-SiC are short-ranged [19, 28, 50]. Previous work on NV$^-$ has shown that forces on atoms that are separated from the defect by more than 5 Å yield a negligible contribution to the HRF [28]. For VV^0 centers, we compared results for the HRF and spectral density using forces from a $(7 \times 7 \times 2)$ supercell and those from a $(5 \times 5 \times 2)$ supercell (see Fig. S7 of the SI). We found a difference less than 5% in the HRFs and the spectral densities are almost identical. In order to obtain phonon frequencies and modes for large supercells, we employed the force constant matrix embedding approach [19], and details can be found in Sec. V of the SI.

The HRFs computed in the dilute limit for NV$^-$ $((12\times12\times12)$ supercell) and VV^0 centers $((16 \times 16 \times 5)$ supercell) differ by 2% and 5-15% respectively, relative to those obtained with $(4 \times 4 \times 4)$ and $(5 \times 5 \times 2)$ supercells. Computed HRFs for NV$^-$ are in close agreement with

18

previous theoretical predictions [19, 22, 28] and experiments [35]. Computed HRFs for VV^0 centers are also in close agreement with our experiments. A previous theoretical work by Hashemi et al. [33] reported a HRF of 2.75 for hh-VV^0. This value falls in the range of our results computed with the $(5 \times 5 \times 2)$ supercell and is 15% smaller than our experimental value likely due to finite size effects not being fully taken into account in Ref. [33]. In the dilute limit, we found that the spectral densities are smoother and exhibit a linear tail below 20 meV, reflecting the coupling with long-range acoustic phonons. Detailed analysis of spectral densities and vibrational modes can be found in Sec. VI of the SI.

C.   Photoluminescence line shapes and Debye-Waller factors

In Fig. 6 we show the PL line shapes computed using the generating function approach (Eq. 7) with HRFs computed at different levels of theory and different supercell sizes, compared with experiment. The spectra consist of a sharp ZPL and a structured PSB. The broadening of the PSB is $\sim$500 meV for NV^- and $\sim$300 meV for VV^0 centers. Note that PL line shapes computed with small supercells show sharper peaks and a gap of 5-10 meV between the ZPL and the PSB. The peaks located at 30 (23) meV from the ZPL for NV^- (hk-VV^0) also stem from finite size effects. In our calculations, the contribution of the e type phonons is computed using the HR theory, which was shown to represent an accurate approximation in the recent work by Razinkovas et al. [28]. These authors computed the contribution of e type phonons to the PL and absorption line shapes for NV^- by explicitly solving the multi-mode $E \otimes e$ Jahn-Teller problem; they showed that if the HRF of e type phonons lies between 0.5 and 1.0, then the HR theory yields reasonable results for the PL line shape. For the NV^- and VV^0 centers, we find a HRF of e type phonons of about 0.5 and 1.0, respectively, indicating that the HR theory should be accurate.

We find that computed and measured line shapes agree well, both in terms of the peak positions and intensity of line shapes, when calculations are performed with the largest supercells $((12 \times 12 \times 12)$ for NV^- and $(16 \times 16 \times 5)$ supercell for VV^0 centers). When computing phonons with the PBE functional, we find that the PSB is clearly dominated by coupling with the 63 meV phonon for NV^-, close to the experimental value 64 meV [35]. The PSB also shows peaks at 122 meV, 135 meV, 150 meV and 161 meV from the ZPL, in good agreement with the experimental values 122 meV, 138 meV, 153 meV and 163 meV [35]. As
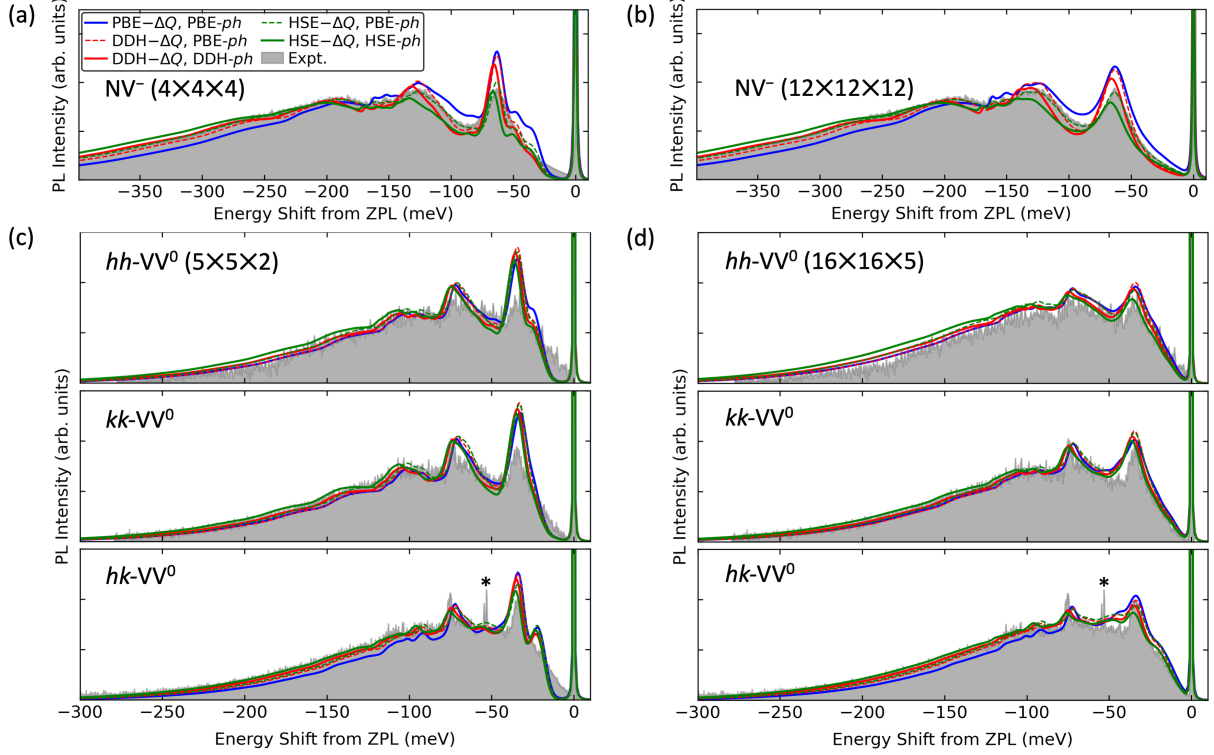
19

FIG. 6. Photoluminescence (PL) line shapes computed at different levels of theory at low temperature (8 K for the NV^- center in diamond and 10 K for VV^0 centers in 4H-SiC). The labels follow the same notation as in Tab. II. We used $\lambda = 0.3$ (0.1) meV in Eq. 8 for the NV^- center (VV^0 centers) to reproduce the experimental broadening of the zero-phonon line. The experimental data for the NV^- center in diamond are from Ref. [19]. The small peak marked with a star '$*$' in the experimental curve is the ZPL of another center and should be disregarded in the comparison between theory and experiment presented here. The intensity of the experimental line shapes has been scaled to match the peaks of the computed line shapes.

for the relative intensity of peaks, the best agreement with experiment is obtained using HSE for the calculation of ΔQ and PBE phonons, respectively. When phonons are computed at the DDH (HSE) level, the 63 meV peak is shifted to 66 (67) meV, and the 161 meV peak to 168 (170) meV. Overall the agreement with experiment is good in all cases.

Similar conclusions can be drawn for the VV^0 centers. When computing phonons with PBE, we obtain peak positions at 34 meV and 72 meV from the ZPL in the PSB, in good agreement with experiments. Calculated PSB also exhibits small peaks located at 90 meV from the ZPL, originating from the coupling with high energy phonons. As for

20

the relative intensity of peaks, those computed with DDH ΔQ or HSE ΔQ are in slightly better agreement with experiments than with PBE, but generalizations to other defects or materials are difficult to make. When computing phonons with the DDH or HSE functionals, the peaks are slightly shifted to lower energy by 1-3 meV, depending on the peak and the agreement with experiments is improved, although again in all cases we find good agreement with the measured spectra. We emphasize that the ability to resolve phonon side bands is important in order to build predictive capabilities to identify fingerprints of defects using first principle calculations.

From the PL line shape we can obtain the DWF, which is defined as the ratio of the emitted light from the ZPL to the total emitted light. At very low temperature, the DWF is computed as DWF $= e^{-S} = e^{-\sum_k S_k}$. In Tab. III we report the DWFs evaluated for the largest supercells. The experimental and theoretical DWFs (see Sec. III B) are in good agreement, and in the case of the VV^0 centers, we find that the computed DWFs show the trend hh-VV^0 < kk-VV^0, consistent with experiments. The relation kk-VV^0 < hk-VV^0 can be reproduced at the PBE level of theory. The computed DWF for hh-VV^0 ranges from 3.6% to 5.3%, smaller than that previously reported, 6.39% [33], likely due to an incomplete finite size extrapolation in Ref. [33]. We also note that a recent experiment on VV^0 centers reported DWFs of 9% and 10% for kk-VV^0 and hk-VV^0 [74], which we consider here to be overestimates, based on our computed and measured spectra. Overall, when using hybrid functionals to compute the GS and ES electronic structure we obtain a good agreement with experiments, with small differences between results for phonons obtained with PBE or hybrid-functionals, provided an extrapolation to the dilute limit is performed.

D. Temperature dependent photoluminescence line shapes

In Fig. 7(a) we show PL line shapes as a function of temperature for NV$^-$. We included the temperature effect on the phonon population and the line shape broadening using Eq. 7. We tuned the parameter λ to obtain the best agreement with experiment; this parameter describes the broadening of the line shape, and is related to the lifetime of the ES and the variation of the local environment of the defect in the experimental samples. The values of λ obtained in our fit to experimental data are reported in the inset of Fig. 7(a). We approximated λ with a quadratic function of T for NV$^-$, consistent with the findings of

TABLE III. Computed Debye-Waller factor (DWF) (%) for spin-conserving transitions using different levels of theory. Results computed with the $(12 \times 12 \times 12)$ supercell for the NV^- center in diamond and $(16 \times 16 \times 5)$ supercell for VV^0 centers in 4H-SiC are shown. We used the same notation as in Tab. II to denote different levels of theory.

Hosts		Diamond		4H-SiC	
Defects		NV^-	hh-VV^0	kk-VV^0	hk-VV^0
PBE$-\Delta Q$	PBE$-ph$	5.0	5.2	7.1	8.5
DDH$-\Delta Q$	PBE$-ph$	4.1	5.3	7.2	6.8
	DDH$-ph$	3.7	4.8	6.6	6.1
HSE$-\Delta Q$	PBE$-ph$	3.0	4.2	6.3	6.2
	HSE$-ph$	2.5	3.6	5.5	5.4
Expt.		3.2 [19]	3.69	6.11	7.54

Ref. [75] for $T \geq 100$ K. We note that the ZPL width was shown to depend on T^5 due to the dynamic Jahn-Teller effect of the ^3E ES for $T \leq 80$ K [73, 76]. The T^5 temperature dependence was not considered in our work due to the lack of experimental data.

Overall, the calculated temperature-dependent PL line shapes agree well with experiments. As the temperature increases, the ZPL width increases due to the decrease of the lifetime of the ES. The intensity of the PSB in the 30 meV range around the ZPL also increases, indicating an increasing population of the higher vibrational levels of the ES long-range modes. The increasing population causes the broadening and the small shift of the first peak of the PSB (about 63 meV lower than ZPL) towards lower energies, as observed both theoretically and experimentally. As for the PSB with energy higher than the ZPL, we find that a shoulder peak at about 60 meV becomes increasingly more intense as the temperature increases, due to the coupling with the quasi-local mode in the ES. Temperature effects on the electronic structure, atomic structure and lattice parameters were neglected in our calculations. These effects are assumed to be relatively small considering the ~3 meV shift of the ZPL from 8 K to 300 K observed in experiments.

The measured and computed temperature-dependent PL line shapes for kk-VV^0 (Fig. 7(b)) are in general good agreement. Also in this case, we observe a broadening of the ZPL and the PSB and the increase of the intensity around the ZPL as the temperature increases.
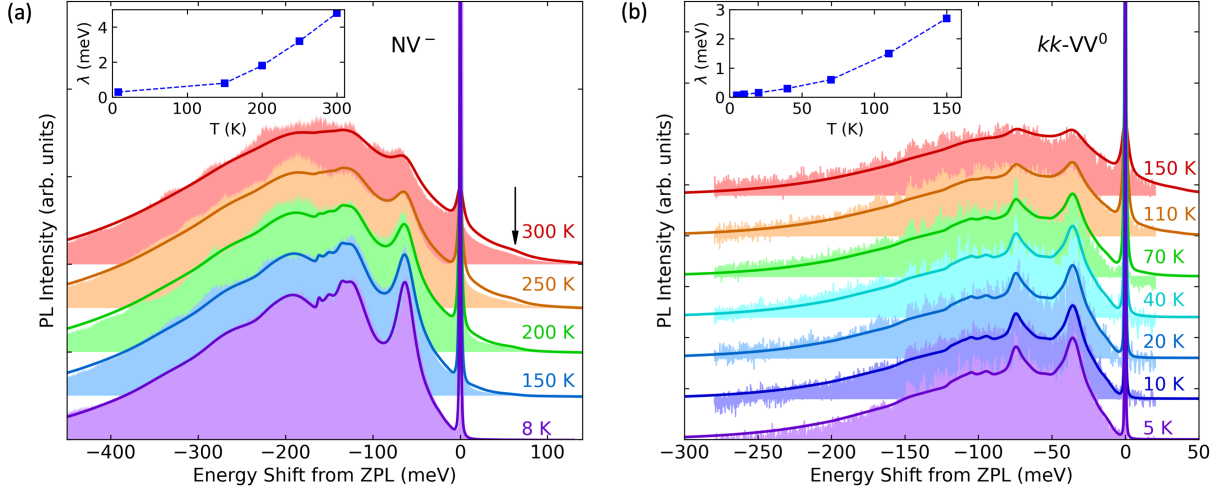
FIG. 7. Computed photoluminescence (PL) line shapes (solid lines) of (a) the NV$^-$ center in diamond and (b) the kk-VV^0 center in 4H-SiC as a function of temperature. The best agreement with experiments is obtained when Huang-Rhys factors (HRFs) are calculated with HSE$-\Delta Q$ and PBE$-ph$ (DDH$-\Delta Q$ and DDH$-ph$) for the NV$^-$ center (kk-VV^0 center) (see Tab. II). The experimental line shapes of the NV$^-$ center are averaged over twenty measurements at 8 K and 300 K and over two measurements at 150 K, 200 K and 250 K in (a). The 8 K data for the NV$^-$ center in diamond in (a) is from Ref. [19]. The broadening parameter λ used in Eq. 8 for the theoretical line shapes is shown in the insets as a function of temperature. The black arrow in (a) indicates a shoulder at approximately 60 meV.

The chosen broadening parameter λ turns out to be a non-linear function of the temperature. Our temperature dependent results show that converged calculations can successfully discern features in the PSB also as a function of T.

E. Displaced harmonic oscillator and the Franck-Condon approximations

We have presented results for PL line shapes obtained using the generating function approach (Eq. 8), which in turn was derived using the FC and the DHO approximations. The former assumes that the transition dipole moment $|\boldsymbol{\mu}_{eg}|$ is independent of changes in the atomic structure, and the latter assumes that the vibrational modes of the GS and the ES are identical except for a displacement. We present below an analysis of the validity of these two approximations using a one-dimensional (1D) model, where just one effective

23

phonon mode is considered. Previous studies have shown that the 1D model provides an accurate description of defect systems with strong electron-phonon coupling (HRF $\gg$ 1) and serves as a valuable approximation to cases with weak or intermediate electron-phonon coupling [8, 10]. The systems considered in this work, e.g., NV$^-$ and kk-VV^0, yield HRF $\approx$ 3 (intermediate electron-phonon coupling); hence the use of the 1D model appears to be justified, although the Herzberg-Teller (HT) effect of symmetry forbidden vibrational modes and the Duschinsky rotation effect between vibrational modes of the GS and the ES [77] are not captured by the model.

In the 1D model, we considered one effective phonon mode which includes only vibrations projected along the direction of the configuration coordinate Q, which connects the equilibrium atomic structures of the GS and the ES (see Fig. 1). The frequency of such effective phonon mode is calculated as the weighted average over all phonon frequencies in either the GS or the ES:

$$\Omega_{\{e,g\}} = \frac{\sum_k \omega_{\{e,g\};k}^2 \Delta Q_k^2}{\sum_k \Delta Q_k^2}. \tag{16}$$

At the PBE level of theory we obtain: for NV$^-$, $\Omega_g = 63.06$ meV, $\Omega_e = 66.38$ meV, and $\Delta Q = \sqrt{\sum_k \Delta Q_k^2} = 0.653$ amu$^{0.5}$ Å; for kk-VV^0, $\Omega_g = 38.11$ meV, $\Omega_e = 43.45$ meV, and $\Delta Q = 0.763$ amu$^{0.5}$ Å. With these parameters we can also compute the HRF for the 1D model as HRF $= \frac{\Omega_g \Delta Q^2}{2\hbar}$. We obtained 3.22 (2.65) for NV$^-$ (kk-VV^0), close to the HRF from the all-phonon calculation with the $(4 \times 4 \times 4)$ $((5 \times 5 \times 2))$ supercell, which is 2.94 (2.51).

Fig. 8(a) shows the PL spectra of NV$^-$ and kk-VV^0 computed using the 1D model with (i) actual Ω_g different from Ω_e, (ii) Ω_g the same as Ω_e and (iii) Ω_e the same as Ω_g. We find that for the NV$^-$ center, the approximation (iii) yields 2.3% and 3.1% relative error at $T = 10$ K and at $T = 300$ K relative to (i). This result agrees with those reported by Razinkovas et al. [28]. In the case of the kk-VV^0 center, the approximation (iii) yields a 6.0% and 9.5% relative error at $T = 10$ K and at $T = 300$ K, respectively, arising from the greater difference between Ω_g and Ω_e. The error caused by using (iii) increases as a function of T, since the number of excited vibrational states contributing to the PL spectrum increases. Since excited vibrational states are more likely to be populated in kk-VV^0 than in NV$^-$, due to the smaller effective phonon frequency, the error is larger for the former. The DHO approximation used in the calculations of PL line shapes in Sec. IV C corresponds to case (iii). Our analysis with the 1D model suggests that the DHO approximation used in our calculations is fairly accurate. In general, we expect the DHO approximation to be valid
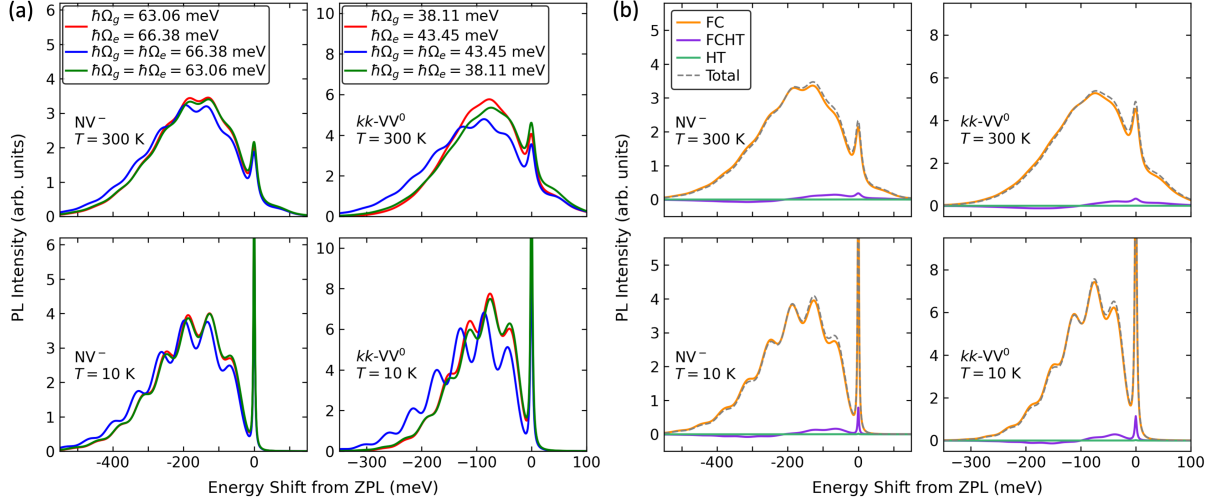
FIG. 8. PL line shapes evaluated within the 1D model for the NV⁻ center in diamond and the kk-VV^0 center in 4H-SiC at $T = 10$ K and $T = 300$ K. (a) Analysis of the the displaced harmonic oscillator (DHO) approximation. Red lines denote the line shapes computed with both the ground state (GS) and the excited state (ES) frequency. Blue (green) lines denote the line shapes computed with DHO approximation using the ES (GS) frequency. (b) 'FC', 'FCHT', and 'HT' denote the contribution to the PL given by the Franck-Condon, Franck-Condon Herzberg-Teller, and the Herzberg-Teller terms, respectively. 'Total' denotes the sum of three terms. The zero-phonon line is broadened using a Lorentzian function with scale parameter λ, and the phonon sideband is broadened using a Gaussian function with standard deviation σ. For the NV⁻ center, $\lambda = 2$ (10) meV and $\sigma = 25$ (30) meV were used at $T = 10$ (300) K. For the kk-VV^0 center, $\lambda = 2$ (8) meV and $\sigma = 15$ (20) meV were used at $T = 10$ (300) K.

for defects in rigid materials with relatively small structural displacements upon optical transitions at low temperature.

In order to use the 1D model to examine the validity of the FC approximation, we first write Eq. 1 without using the FC principle:

$$L(\hbar\omega, T) \propto \omega^3 \sum_i \sum_j P_{ej}(T) |\langle \Theta_{ej} | \boldsymbol{\mu}_{eg} | \Theta_{gi} \rangle|^2 \delta\left(E_{\mathrm{ZPL}} + E_{ej} - E_{gi} - \hbar\omega\right). \qquad (17)$$

Within the 1D effective phonon approximation we have:

$$\langle \Theta_{ej} | \boldsymbol{\mu}_{eg} | \Theta_{gi} \rangle = \int dQ \, \phi^*_{n^{ej}}(Q) \boldsymbol{\mu}_{eg}(Q) \phi_{n^{gi}}(Q). \qquad (18)$$

Here we use the same notations for nuclear wavefunctions and vibrational states as in Eq. 3. The quantity $\boldsymbol{\mu}_{eg}(Q) = \langle \psi_e(Q) | \hat{\boldsymbol{\mu}} | \psi_g(Q) \rangle$ is the transition dipole moment between electronic

wavefunctions obtained at fixed values of the configuration coordinate Q, where ψ_e (ψ_g) is the electronic wavefunction of the system in the ES (GS). To first order in Q we can further approximate Eq. 18 as:

$$\langle \Theta_{ej} | \boldsymbol{\mu}_{eg} | \Theta_{gi} \rangle \approx \boldsymbol{\mu}_{eg}(Q=0)\langle \phi_{n^{ej}} | \phi_{n^{gi}} \rangle + \frac{d\boldsymbol{\mu}_{eg}}{dQ}\bigg|_{Q=0} \langle \phi_{n^{ej}} | Q | \phi_{n^{gi}} \rangle \qquad (19)$$

We have numerically computed the electronic transition dipole moment as a function of Q, and verified that the dependence is linear with a relative change of about 10% between the equilibrium atomic structures of GS and ES for both NV$^-$ and kk-VV^0 (see Fig. S12 of the SI).

After introducing Eq. 19 in Eq. 17 we recognize the usual FC term, and the terms beyond the FC approximation. The latter can be grouped into two categories: the Franck-Condon Herzberg-Teller (FCHT), and the Herzberg-Teller (HT) term, depending on whether one or two derivatives of the electronic transition dipole moment with respect to Q are present, respectively (see Eq. S13-S15 of the SI). Fig. 8(b) shows the FC, FCHT, and HT contributions to the PL line shape for both NV$^-$ and kk-VV^0, at $T = 10$ K and $T = 300$ K. We find that the FC term is the dominant one and that the FCHT and HT contributions are smaller than 5% and 0.1% of the total intensity, respectively. These results indicate that the FC approximation used in Sec. IV C is accurate. We note that the validity of the FC approximation depends on the symmetry and the strength of electron-phonon coupling of the defect center. For negatively-charged silicon vacancy centers in diamond, the HT term may not be negligible [24, 50]. We suggest that computing the relative error caused by neglecting FCHT and HT contributions using the 1D model is a useful first step in assessing the validity of the FC approximation.

V.   CONCLUSIONS

In summary, we presented a detailed comparison of measured and computed PL spectra of defects in diamond and SiC, aimed at assessing the validity of theoretical and numerical approximations used in first principles calculations. As expected, our results show that the best agreement between theory and experiments is obtained when using hybrid functionals, instead of PBE, although the qualitative differences between the PL line shapes of the different configurations of the VV^0 centers are reproduced with PBE as well. We find minor

differences between the results obtained with the hybrid functionals HSE and DDH: the values of the ZPL obtained with the two functionals are almost identical (note that our HSE results slightly differ from previous ones reported in the literature for the case of the NV^-) and the values of the HRF differ by less than 10%. We also find minor differences between spectral densities computed at the PBE and DDH level of theory, indicating that the major improvement of hybrid functionals over PBE is in the determination of the electronic structure of the system. Our findings show that results for the triplet ES obtained with CDFT and TDDFT are similar at the DDH level of theory for NV^- and VV^0 centers, suggesting that the relatively cheap CDFT method is accurate for the calculations of their PL spectra. In addition, by using a 1D model, we provided a qualitative assessment of the approximation arising from the use of the FC principle and of the DHO approximation, finding that both of them are justified. Finally, we emphasize the importance of finite size scaling to obtain theoretical results in agreement with experiments for HRFs and PL line shapes, especially for the contribution of quasi-local and long-range acoustic phonon modes. The protocol established in our work shows that accurate results for PL spectra may be obtained at a given temperature using the generating function approach, with phonons extrapolated to the dilute limit, and by using hybrid functionals to compute the GS and ES potential energy surfaces of the defects, with the ES computed with constrained DFT. A 1D model can be used to evaluate the accuracy of the FC and DHO approximations. This protocol, validated here for NV^- and VV^0 centers, leads to robust predictions of the overall line shape, including PSBs, which can be used to aid the identification and characterization of optically-active defects.

---

[1] F. J. Heremans, C. G. Yale, and D. D. Awschalom, Proc. IEEE **104**, 2009 (2016).

[2] D. D. Awschalom, R. Hanson, J. Wrachtrup, and B. B. Zhou, Nat. Photonics **12**, 516 (2018).

[3] G. Zhang, Y. Cheng, J.-P. Chou, and A. Gali, Appl. Phys. Rev. **7**, 031308 (2020).

[4] G. Wolfowicz, F. J. Heremans, C. P. Anderson, S. Kanai, H. Seo, A. Gali, G. Galli, and D. D. Awschalom, Nat. Rev. Mater. (2021).

[5] J. Walker, Rep. Prog. Phys. **42**, 1605 (1979).

[6] K. Huang, A. Rhys, and N. F. Mott, Proc. R. Soc. Lond. Series A **204**, 406 (1950).

[7] C. Freysoldt, B. Grabowski, T. Hickel, J. Neugebauer, G. Kresse, A. Janotti, and C. G. Van de Walle, Rev. Mod. Phys. **86**, 253 (2014).

[8] A. Alkauskas, M. D. McCluskey, and C. G. Van de Walle, J. Appl. Phys. **119**, 181101 (2016).

[9] C. E. Dreyer, A. Alkauskas, J. L. Lyons, A. Janotti, and C. G. Van de Walle, Annu. Rev. Mater. Res. **48**, 1 (2018).

[10] A. Alkauskas, J. L. Lyons, D. Steiauf, and C. G. Van de Walle, Phys. Rev. Lett. **109**, 267401 (2012).

[11] M. A. Reshchikov, J. Appl. Phys. **129**, 121101 (2021).

[12] I. A. Aleksandrov and K. S. Zhuravlev, J. Phys. Condens. Matter **32**, 435501 (2020).

[13] S. A. Tawfik, S. Ali, M. Fronzi, M. Kianinia, T. T. Tran, C. Stampfl, I. Aharonovich, M. Toth, and M. J. Ford, Nanoscale **9**, 13575 (2017).

[14] H. Hamdi, G. Thiering, Z. Bodrog, V. Ivdy, and A. Gali, NPJ Comput. Mater. **6**, 178 (2020).

[15] G. Grosso, H. Moon, C. J. Ciccarino, J. Flick, N. Mendelson, L. Mennel, M. Toth, I. Aharonovich, P. Narang, and D. R. Englund, ACS Photonics **7**, 1410 (2020).

[16] R. Camphausen, L. Marini, S. A. Tawfik, T. T. Tran, M. J. Ford, and S. Palomba, APL Photonics **5**, 076103 (2020).

[17] C. Jara, T. Rauch, S. Botti, M. A. L. Marques, A. Norambuena, R. Coto, J. E. Castellanos-guila, J. R. Maze, and F. Munoz, J. Phys. Chem. A **125**, 1325 (2021).

[18] C. Linderälv, W. Wieczorek, and P. Erhart, Phys. Rev. B **103**, 115421 (2021).

[19] A. Alkauskas, B. B. Buckley, D. D. Awschalom, and C. G. Van de Walle, New J. Phys. **16**, 073026 (2014).

[20] G. Thiering and A. Gali, Phys. Rev. B **92**, 165203 (2015).

[21] A. Norambuena, S. A. Reyes, J. Mejía-Lopéz, A. Gali, and J. R. Maze, Phys. Rev. B **94**, 134305 (2016).

[22] G. Thiering and A. Gali, Phys. Rev. B **96**, 081115 (2017).

[23] J. Zhang, C.-Z. Wang, Z. Zhu, Q. H. Liu, and K.-M. Ho, Phys. Rev. B **97**, 165204 (2018).

[24] G. Thiering and A. Gali, Phys. Rev. X **8**, 021063 (2018).

[25] I. Harris, C. J. Ciccarino, J. Flick, D. R. Englund, and P. Narang, Phys. Rev. B **102**, 195206 (2020).

[26] A. Karim, I. Lyskov, S. P. Russo, and A. Peruzzo, J. Appl. Phys. **128**, 233102 (2020).

[27] M. R. Zemła, K. Czelej, P. Kamińska, C. G. Van de Walle, and J. A. Majewski, Phys. Rev. B **102**, 115102 (2020).

[28] L. Razinkovas, M. W. Doherty, N. B. Manson, C. G. Van de Walle, and A. Alkauskas, Phys. Rev. B **104**, 045303 (2021).

[29] A. Karim, I. Lyskov, S. P. Russo, and A. Peruzzo, Bright ab-initio photoluminescence of NV^+ in diamond (2021), arXiv:2104.04256 [cond-mat.mes-hall].

[30] P. Udvarhelyi, G. Thiering, N. Morioka, C. Babin, F. Kaiser, D. Lukin, T. Ohshima, J. Ul-Hassan, N. T. Son, J. Vučković, J. Wrachtrup, and A. Gali, Phys. Rev. Applied **13**, 054017 (2020).

[31] Z. Shang, A. Hashemi, Y. Berencén, H.-P. Komsa, P. Erhart, S. Zhou, M. Helm, A. V. Krasheninnikov, and G. V. Astakhov, Phys. Rev. B **101**, 144109 (2020).

[32] Q. Hassanzada, I. A. Sarsari, A. Hashemi, A. Ghojavand, A. Gali, and M. Abdi, Phys. Rev. B **102**, 134103 (2020).

[33] A. Hashemi, C. Linderälv, A. V. Krasheninnikov, T. Ala-Nissila, P. Erhart, and H.-P. Komsa, Phys. Rev. B **103**, 125203 (2021).

[34] C. Chakraborty, C. J. Ciccarino, and P. Narang, Dynamic modulation of phonon-assisted transitions in quantum defects in monolayer transition-metal dichalcogenide semiconductors

(2020), arXiv:2007.14399 [cond-mat.mtrl-sci].

[35] P. Kehayias, M. W. Doherty, D. English, R. Fischer, A. Jarmola, K. Jensen, N. Leefer, P. Hemmer, N. B. Manson, and D. Budker, Phys. Rev. B **88**, 165202 (2013).

[36] R. Schirhagl, K. Chang, M. Loretz, and C. L. Degen, Annu. Rev. Phys. Chem. **65**, 83 (2014).

[37] M. W. Doherty, N. B. Manson, P. Delaney, F. Jelezko, J. Wrachtrup, and L. C. Hollenberg, Phys. Rep. **528**, 1 (2013).

[38] A. Gali, Nanophotonics **8**, 1907 (2019).

[39] Z. Su, Z. Ren, Y. Bao, X. Lao, J. Zhang, J. Zhang, D. Zhu, Y. Lu, Y. Hao, and S. Xu, J. Mater. Chem. C **7**, 8086 (2019).

[40] G. Wolfowicz, C. P. Anderson, A. L. Yeats, S. J. Whiteley, J. Niklas, O. G. Poluektov, F. J. Heremans, and D. D. Awschalom, Nat. Commun. **8**, 1 (2017).

[41] D. J. Christle, P. V. Klimov, C. F. de las Casas, K. Szász, V. Ivády, V. Jokubavicius, J. Ul Hassan, M. Syväjärvi, W. F. Koehl, T. Ohshima, N. T. Son, E. Janzén, A. Gali, and D. D. Awschalom, Phys. Rev. X **7**, 021046 (2017).

[42] J. Davidsson, V. Ivády, R. Armiento, N. T. Son, A. Gali, and I. A. Abrikosov, New J. Phys. **20**, 023035 (2018).

[43] N. T. Son, C. P. Anderson, A. Bourassa, K. C. Miao, C. Babin, M. Widmann, M. Niethammer, J. Ul Hassan, N. Morioka, I. G. Ivanov, F. Kaiser, J. Wrachtrup, and D. D. Awschalom, Appl. Phys. Lett. **116**, 190501 (2020).

[44] A. Gali, E. Janzén, P. Deák, G. Kresse, and E. Kaxiras, Phys. Rev. Lett. **103**, 186404 (2009).

[45] J. Sun, J. Yang, and C. A. Ullrich, Phys. Rev. Research **2**, 013091 (2020).

[46] S. S. Dong, M. Govoni, and G. Galli, Chem. Sci. **12**, 4970 (2021).

[47] A. Gali, Phys. Status Solidi B **248**, 1337 (2011).

[48] A. Petrone, J. J. Goings, and X. Li, Phys. Rev. B **94**, 165402 (2016).

[49] A. Petrone, R. A. Beck, J. M. Kasper, X. Li, Y. Huang, M. Crane, and P. Pauzauskie, Phys. Rev. B **98**, 205405 (2018).

[50] E. Londero, G. Thiering, L. Razinkovas, A. Gali, and A. Alkauskas, Phys. Rev. B **98**, 035306 (2018).

[51] L. Råde and B. Westergren, *Mathematics handbook for science and engineering*, Vol. 4 (Springer, 1995).

[52] M. Lax, J. Chem. Phys. **20**, 1752 (1952).

[53] R. Kubo and Y. Toyozawa, Prog. Theor. Phys. **13**, 160 (1955).

[54] P. Giannozzi, S. Baroni, N. Bonini, M. Calandra, R. Car, C. Cavazzoni, D. Ceresoli, G. L. Chiarotti, M. Cococcioni, I. Dabo, A. Dal Corso, S. de Gironcoli, S. Fabris, G. Fratesi, R. Gebauer, U. Gerstmann, C. Gougoussis, A. Kokalj, M. Lazzeri, L. Martin-Samos, N. Marzari, F. Mauri, R. Mazzarello, S. Paolini, A. Pasquarello, L. Paulatto, C. Sbraccia, S. Scandolo, G. Sclauzero, A. P. Seitsonen, A. Smogunov, P. Umari, and R. M. Wentzcovitch, J. Phys.: Condens. Matter **21**, 395502 (2009).

[55] P. Giannozzi, O. Andreussi, T. Brumme, O. Bunau, M. B. Nardelli, M. Calandra, R. Car, C. Cavazzoni, D. Ceresoli, M. Cococcioni, N. Colonna, I. Carnimeo, A. D. Corso, S. de Gironcoli, P. Delugas, R. A. D. Jr, A. Ferretti, A. Floris, G. Fratesi, G. Fugallo, R. Gebauer, U. Gerstmann, F. Giustino, T. Gorni, J. Jia, M. Kawamura, H.-Y. Ko, A. Kokalj, E. Kkbenli, M. Lazzeri, M. Marsili, N. Marzari, F. Mauri, N. L. Nguyen, H.-V. Nguyen, A. O. de-la Roza, L. Paulatto, S. Ponc, D. Rocca, R. Sabatini, B. Santra, M. Schlipf, A. P. Seitsonen, A. Smogunov, I. Timrov, T. Thonhauser, P. Umari, N. Vast, X. Wu, and S. Baroni, J. Phys.: Condens. Matter **29**, 465901 (2017).

[56] P. Giannozzi, O. Baseggio, P. Bonf, D. Brunato, R. Car, I. Carnimeo, C. Cavazzoni, S. de Gironcoli, P. Delugas, F. Ferrari Ruffino, A. Ferretti, N. Marzari, I. Timrov, A. Urru, and S. Baroni, J. Chem. Phys. **152**, 154105 (2020).

[57] D. R. Hamann, Phys. Rev. B **88**, 085117 (2013).

[58] M. Schlipf and F. Gygi, Comput. Phys. Commun. **196**, 36 (2015).

[59] J. P. Perdew, K. Burke, and M. Ernzerhof, Phys. Rev. Lett. **77**, 3865 (1996).

[60] J. H. Skone, M. Govoni, and G. Galli, Phys. Rev. B **89**, 195112 (2014).

[61] J. Heyd, G. E. Scuseria, and M. Ernzerhof, J. Chem. Phys. **118**, 8207 (2003).

[62] J. Heyd, G. E. Scuseria, and M. Ernzerhof, J. Chem. Phys. **124**, 219906 (2006).

[63] H. Seo, H. Ma, M. Govoni, and G. Galli, Phys. Rev. Materials **1**, 075002 (2017).

[64] See supplemental material at [url will be inserted by publisher] for (i) properties of bulk diamond and 4H-SiC; (ii) details of CDFT calculations; (iii) atomic displacements upon optical excitation; (iv) phonons at the level of hybrid functionals; (v) details of extrapolating to the dilute limit; (vi) detailed analysis of spectral densities and vibrational modes analysis; (vii) calculations of transition dipole moment and radiative lifetime. (2021).

[65] L. Gordon, A. Janotti, and C. G. Van de Walle, Phys. Rev. B **92**, 045208 (2015).

[66] M. Govoni and G. Galli, J. Chem. Theory Comput. **11**, 2680 (2015).

[67] N. L. Nguyen, H. Ma, M. Govoni, F. Gygi, and G. Galli, Phys. Rev. Lett. **122**, 237402 (2019).

[68] A. Togo and I. Tanaka, Scr. Mater. **108**, 1 (2015).

[69] M. Mackoit-Sinkeviien, M. Maciaszek, C. G. Van de Walle, and A. Alkauskas, Appl. Phys. Lett. **115**, 212101 (2019).

[70] H. Ma, M. Govoni, and G. Galli, npj. Comput. Mater. **6**, 85 (2020).

[71] H. Ma, N. Sheng, M. Govoni, and G. Galli, Phys. Chem. Chem. Phys. **22**, 25522 (2020).

[72] H. Ma, N. Sheng, M. Govoni, and G. Galli, J. Chem. Theory Comput. **17**, 2116 (2021), pMID: 33739106.

[73] T. A. Abtew, Y. Y. Sun, B.-C. Shih, P. Dev, S. B. Zhang, and P. Zhang, Phys. Rev. Lett. **107**, 146403 (2011).

[74] Z. Shang, Y. Berencén, M. Hollenbach, S. Zhou, H. Kraus, T. Ohshima, and G. Astakhov, Phys. Rev. Applied **15**, 034059 (2021).

[75] M. Fukami, C. Yale, P. Andrich, X. Liu, F. Heremans, P. Nealey, and D. Awschalom, Phys. Rev. Applied **12**, 014042 (2019).

[76] K.-M. C. Fu, C. Santori, P. E. Barclay, L. J. Rogers, N. B. Manson, and R. G. Beausoleil, Phys. Rev. Lett. **103**, 256404 (2009).

[77] F. Duschinsky, Acta Physicochim. (URSS) **7**, 551 (1937).